Continuum Mech. Thermodyn. (2000) 12: 289–301

Characteristic waves and dissipation in the 13-moment-case

M. Torrilhon*

Institut für Verfahrenstechnik, TU Berlin, Fasanenstrasse 90, 10623 Berlin, Germany

Received April 13, 2000

Extended thermodynamics derives dissipative, hyperbolic field equations for monatomic gases. One example is the system of the 13-field-case, which is a dissipative extension of the Euler equations. In this paper the system is investigated by solving a Riemann problem. Additionally some model equations are introduced so as to discuss the main properties in a transparent manner. There arises an interesting interplay of the characteristic waves and the dissipation in the system.

For the 13-field-case it turns out that not every Riemann problem has a solution, because of the loss of hyperbolicity of the system.

1 Introduction

The equations in this paper may be derived in the context of extended thermodynamics for momatomic ideal gases [1]. In extended thermodynamics the ordinary set of variables, density, momentum and energy is extended by the stress tensor, the heat flux and so-called higher moments, which do not have an intuitive physical meaning. The main idea is, that in the case of processes with strong gradients and rapid changes many variables are necessary for an appropriate theoretical description ([1], [2]).

The constitutive theory of extended thermodynamics yields dissipative, symmetric hyperbolic field equations for a special choice of variables. The system may be written in the form

$$\frac{\partial u}{\partial t} + \frac{\partial f(u)}{\partial x} = P(u) \ , \tag{1}$$

where the homogeneous part is hyperbolic and the productions $P(u)$ are algebraic. The first components of $P(u)$ vanish identically, indicating the conservation of mass, momentum and energy. Systems like (1) are also called conservation laws with relaxation (see [3]).

The simplest choice of variables takes into account density, momentum and energy and leads to the Euler equations of gas dynamics. If this set of variables is extended by the stress tensor and the heat flux we obtain Grad's 13-moment-system, which is dissipative contrary to the Euler equations. Larger sets of variables will not be used in this paper.

In this paper the emphasis is not on the physical but on the mathematical properties of the 13-field-case, namely the interaction of the characteristic waves and the dissipation in the system. The Riemann problem, that is an initial value problem of the type

$$u(x, t = 0) = \begin{cases} u_l = const & x \leq 0 \\ u_r = const & x > 0 \end{cases} \ , \tag{2}$$

* e-mail: M.Torrilhon@vt.tu-berlin.de

will be solved numerically. These initial conditions induce a typical set of waves depending on the characteristic structure of the system. The waves of the 13-field-case will be discussed in comparison with the waves of the Euler-case.

2 Field equations

The derivation of the field equations is presented and discussed in [1]. Here only the result and some properties are displayed.

2.1 Euler case

The Euler equations are written here in the variables density ρ, velocity v_i and pressure p. We restrict the attention to the one-dimensional case. Thus there are three equations which read ($v \equiv v_1$)

$$\begin{aligned} \frac{\partial \rho}{\partial t} + \frac{\partial \rho v}{\partial x} &= 0\,, \\ \frac{\partial \rho v}{\partial t} + \frac{\partial}{\partial x}\left(\rho v^2 + p\right) &= 0\,, \\ \frac{\partial}{\partial t}\left(\rho v^2 + 3p\right) + \frac{\partial}{\partial x}\left(\rho v^3 + 5pv\right) &= 0\,. \end{aligned} \tag{3}$$

These represent the non-dissipative balance equations for mass, momentum and energy. All quantities should be viewed as dimensionless. For scaling density and pressure I used a reference state ρ_0, p_0 and for the velocity Newton's speed of sound $\sqrt{p_0/\rho_0}$. The scales of time and space obey $x_0/t_0 = \sqrt{p_0/\rho_0}$.

The system (3) is hyperbolic with the three characteristic velocities

$$\lambda_1 = v + \sqrt{\frac{5}{3}\frac{p}{\rho}}\,, \qquad \lambda_2 = v\,, \qquad \lambda_3 = v - \sqrt{\frac{5}{3}\frac{p}{\rho}}\,, \tag{4}$$

which imply three characteristic waves. These waves are well investigated ([4], [5], [6]) and represent the rarefaction wave, the contact discontinuity and the shock which are observed in shock-tube-experiments.

2.2 13-field-case

The set of variables of the Euler equations together with the pressure deviator $p_{\langle ij\rangle}$ (negative deviatoric stress) and the heat flux q_i includes 13 fields. In one dimension we abreviate $\sigma \equiv p_{\langle 11\rangle}$ and $q \equiv q_1$ and the governing system reduces to the five equations

$$\begin{aligned} \frac{\partial \rho}{\partial t} + \frac{\partial \rho v}{\partial x} &= 0\,, \\ \frac{\partial \rho v}{\partial t} + \frac{\partial}{\partial x}\left(\rho v^2 + p + \sigma\right) &= 0\,, \\ \frac{\partial}{\partial t}\left(\rho v^2 + 3p\right) + \frac{\partial}{\partial x}\left(\rho v^3 + 5pv + 2\sigma v + 2q\right) &= 0\,, \\ \frac{\partial}{\partial t}\left(\frac{2}{3}\rho v^2 + \sigma\right) + \frac{\partial}{\partial x}\left(\frac{2}{3}\rho v^3 + \frac{4}{3}pv + \frac{7}{3}\sigma v + \frac{8}{15}q\right) &= -\frac{4}{5}B\,\rho\,\sigma\,, \\ \frac{\partial}{\partial t}\left(\rho v^3 + 5pv + 2\sigma v + 2q\right) + \frac{\partial}{\partial x}\left(\rho v^4 + 8pv^2 + 5\sigma v^2 + \frac{32}{5}qv + \frac{p}{\rho}(5p + 7\sigma)\right) &= -\frac{8}{5}B\,\rho\left(\frac{2}{3}q + \sigma v\right). \end{aligned} \tag{5}$$

The system is scaled like the Euler equations (4). The scales used for the stress σ and the heat flux q are p_0 and $p_0\sqrt{p_0/\rho_0}$. The productions of the last two equations have been calculated from the collision operator of the Boltzmann equation under the assumption of a particle interaction with a Maxwell-potential. There

appears the mean time of free flight τ_0 of the particles in the reference state. This quantity leads to the parameter B in (5)

$$B = \frac{\text{observation time scale } t_0}{\text{mean time of free flight } \tau_0} \sim \frac{\text{observation length scale } x_0}{\text{mean free path } \lambda_0} = \frac{1}{Kn} , \tag{6}$$

which is essentially the inverse of the Knudsen number. This parameter controls the influence of the productions and thus of the dissipation; its effect will be discussed in the next sections.

The productions vanish in equilibrium, so that we have

$$\sigma = 0 , \qquad q = 0 , \tag{7}$$

which means vanishing deviatoric stress and heat flux. Therefore stress and heat flux are non-equilibrium quantities.

It is remarkable that the Euler equations are formally recovered within the 13-field-case by letting B tend to ∞. The last two equations provide vanishing stress and heat flux and the Euler equations are thus recovered in the first equations. This behavior is typical for the systems derived by extended thermodynamics.

Due to Galilean invariance the characteristic velocities have the representation

$$\lambda = v + \widehat{\lambda}\,(\rho, p, \sigma, q) \tag{8}$$

and we obtain the characteristic polynomial

$$25\rho\widehat{\lambda}^5 + \widehat{\lambda}^3 \left(\frac{310}{3}\sigma - 130p \right) - 96q\,\widehat{\lambda}^2 + \frac{15}{\rho}\left(7\sigma^2 - 10\,\sigma\,p + 5p^2\right)\widehat{\lambda} = 0 \tag{9}$$

for $\widehat{\lambda}$ (see [1]). In equilibrium this equation degenerates to biquadratic form and the characteristic velocities read

$$\lambda_{1,5}|_E = v \pm 1.6503\sqrt{\frac{5}{3}\frac{p}{\rho}} , \qquad \lambda_{2,4}|_E = v \pm 0.6297\sqrt{\frac{5}{3}\frac{p}{\rho}} , \qquad \lambda_3|_E = v . \tag{10}$$

These velocities differ from those in the Euler case (4). It is well known, that the characteristic structure of the Euler equations with its three waves is responsible for the proper description of the physical phenomena. The 13-field-case has a different characteristic structure; in particular there are five waves instead of three. Therefore the question arises wether the 13-field-case is able to describe the phenomena correctly. In the next sections we will see that the dissipation provides a satisfactory answer.

The above system (5) may be brought into conservative form

$$\frac{\partial u}{\partial t} + \frac{\partial f\,(u)}{\partial x} = -B\,P\,(u) \tag{11}$$

with the flux functions

$$\begin{aligned}
f_1 &= u_2 , \\
f_2 &= \frac{1}{3}u_3 + u_4 , \\
f_3 &= u_5 , \\
f_4 &= \frac{4}{15}u_5 + \frac{9}{5}u_4 v - \frac{4}{5}u_2 v^2 , \\
f_5 &= \frac{16}{5}u_5 v - \frac{56}{15}u_4 v^2 - \frac{16}{3}u_3 v^2 + \frac{158}{45}u_2 v^3 + \frac{5}{9}\frac{u_3^2}{u_1} + \frac{7}{3}\frac{u_3 u_4}{u_1}
\end{aligned} \tag{12}$$

and the productions

$$\begin{aligned}
P_{1,2,3} &= 0 , \\
P_4 &= \frac{4}{5}u_1\left(u_4 - \frac{2}{3}u_2 v\right) , \\
P_5 &= \frac{8}{5}u_1\left(\frac{1}{3}u_5 + \frac{1}{3}u_4 v - \frac{5}{9}u_3 v\right) .
\end{aligned} \tag{13}$$

The 13-field-case is subject to testing of numerical methods in [7]. Similar systems have been investigated in [8].

3 Numerical method

The results in this paper were calculated by use of the fortran package CLAWPACK [9]. This package implements a high resolution upwind method ([6], [10]) for the solution of hyperbolic equations in the form (1). It provides several limiter functions from which only the superbee limiter has been used here.

The production terms $P(u)$ are incorporated by an operator splitting after Strang [11], so one has to solve the reduced equation

$$\frac{\partial u}{\partial t} = P(u) \tag{14}$$

over a given time step. In extended thermodynamics these equations are easily solved, since the productions (13) are algebraic and thus the equations (14) form a system of ordinary differential equations which decouple spatially. For the solution either the method of Heun has been applied or - in the case of large B in (11) - an implicit Runge-Kutta-method [12].

As Riemann solver the approximate Roe solver [13] has been utilized. In the case of the Euler equations it is possible to calculate the required Roe matrix A_R and its eigenvalues and eigenvectors analytically. In extended thermodynamics this is not so easily done. As an alternative I have used the integral

$$A_R = \int_0^1 f'(u_l + \theta(u_r - u_l))\, d\theta\,, \tag{15}$$

which is the result of the application of the mean value theorem to the condition $A_R(u_r - u_l) = f(u_r) - f(u_l)$ (see [13]). The quantities u_r and u_l are the right and left states of the local Riemann problem and f' is the Jacobian of the flux function. The integral has been calculated numerically for each Riemann problem by use of the Simpson rule. The eigenvalues and eigenvectors of the resulting Roe matrix were obtained by a routine of the NAG library [14]. This procedure is relatively expensive, but it provides a possibility to use the upwind method for arbitrary hyperbolic equations.

Additionally an entropy-fix has been implemented, based on the approach described in [15], but in the calculations presented here it did not come into play.

The resulting Riemann solver was tested by comparing results with the solutions obtained from usual Riemann solvers for the Euler equations and by using more accurate integration formulas in (15). In all cases considered the differences were not significant.

4 Simple model equations

The equations of the 13-field-case are rather complicated and non-transparent. Some analysis of the waves is done in [1]. In this section we will therefore consider model equations which include several interesting features of the 13-field-case in a much simpler form. These equations and their solutions provide an instructive insight and help to understand the results of the 13-field-case presented in the last section.

The simplest nonlinear hyperbolic equation is the Burgers equation

$$\frac{\partial u}{\partial t} + \frac{\partial \frac{1}{2}u^2}{\partial x} = 0 \tag{16}$$

with the characteristic velocity $\lambda = u$. We will extend the set of variables of the Burgers equation by the variable σ, such that the complete system is hyperbolic and *dissipative* and the Burgers equation is recovered by some limiting process. One possible system like that is

$$\begin{aligned} \frac{\partial u}{\partial t} + \frac{\partial}{\partial x}\left(\frac{1}{2}u^2 + 2\sigma\right) &= 0\,, \\ \frac{\partial \sigma}{\partial t} + \frac{\partial u}{\partial x} &= -B\,\sigma\,. \end{aligned} \tag{17}$$

An ”equilibrium” may be characterized by $\sigma = 0$, so that σ is a non-equilibrium quantity; for $B \to \infty$ the system reduces to the Burgers equation in $(17)_1$.

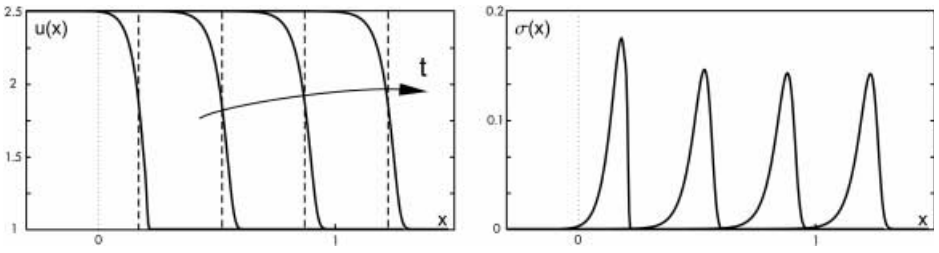

Fig. 1. Travelling wave solution of (17) for different times

The characteristic polynomial of the system is given by

$$\lambda^2 - u\,\lambda - 2 = 0 \tag{18}$$

with the solutions

$$\lambda_{1,2} = \frac{u}{2} \pm \sqrt{\frac{u^2}{4} + 2}\,. \tag{19}$$

Thus we have $\lambda_1 > 0$ and $\lambda_2 < 0$. Like in the 13-field-case these characteristic velocities differ from that of the Burgers equation and the question arises how the solutions of (17) are connected to the soultions of the Burgers equation.

We proceed by investigating a special case.

4.1 Travelling wave

In Fig. 1 the numerical soultion of the Riemann problem with the initial data given by

$$u\,(x, t = 0) = \begin{cases} 2.5 & x \le 0\,, \\ 1 & x > 0\,, \end{cases} \qquad \sigma\,(x, t = 0) = 0 \tag{20}$$

is shown for different times

$$t = 0.1,\ 0.3,\ 0.5,\ 0.7.$$

The parameter B has been chosen as $B = 100$. We see that after a start-up phase a steady profile of a travelling wave appears. The dashed line in Fig. 1 represents the shock solution of the Burgers equation with the initial condition (20). The smooth solution of the system follows the shock solution with a diffusive profile, the *shock* becomes a *shock structure*. The soliton-like solution of σ indicates a "non-equilibrium" through the shock structure. Note that no characteristic wave of the system is observed in Fig.1. It will be shown later on, that these waves have been damped out at the given time.

The shock structure may be calculated from (17) with the travelling wave ansatz

$$u\,(x, t) = \widehat{u}\,(\xi) = \widehat{u}\,(x - vt)\ , \tag{21}$$

$$\sigma\,(x, t) = \widehat{\sigma}\,(\xi) = \widehat{\sigma}\,(x - vt) \tag{22}$$

and the boundary conditions

$$\widehat{u}\,(\pm\infty) = u_{\pm}\ , \tag{23}$$

$$\widehat{\sigma}\,(\pm\infty) = 0\,. \tag{24}$$

In (21)/(22) v is the as yet unknown velocity of the wave. Insertion of (21)/(22) into (17) and integration of equation $(17)_1$ from $-\infty$ to some arbitrary state gives

$$\widehat{\sigma}\,\left(\widehat{u}\right) = \frac{1}{2} v\,(\widehat{u} - u_{-}) - \frac{1}{4}\left(\widehat{u}^2 - u_{-}^2\right)\ . \tag{25}$$

From the boundary condition $\widehat{\sigma}\,(u_{+}) = 0$ the velocity

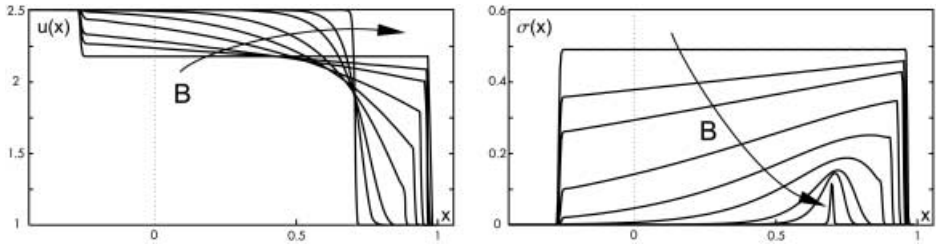

Fig. 2. Solution of (17) for a fixed time and different B

$$v = \frac{u_+ + u_-}{2} \tag{26}$$

is calculated. This is indeed the shock speed of the Burgers equation.

Equation $(17)_2$ with (21)–(26) reduces to

$$\widehat{u}'(\xi) = B\,\frac{\left(\widehat{u} - u_-\right)\left(\widehat{u} - u_+\right)}{v^2 - \widehat{u}\,v - 2}\,, \tag{27}$$

which yields the implicit form of the shock structure

$$\xi\left(\widehat{u}\right) = \frac{2}{u_+ - u_-}\ln\left(\frac{u_+ - \widehat{u}}{\widehat{u} - u_-}\right) + \frac{u_+ + u_-}{4}\ln\left(4\frac{\left(\widehat{u} - u_+\right)\left(\widehat{u} - u_-\right)}{\left(u_+ - u_-\right)^2}\right)\,. \tag{28}$$

The integration constant is chosen so that $\xi\left(\frac{u_+ + u_-}{2}\right) = 0$ holds.

The Burgers equation permits only stable shocks with $u_- > u_+$. This is also reflected in (27): Even if the values for u_- and u_+ are exchanged, the condition $\widehat{u}' < 0$ holds. The system (17) allows only compressional shock structures. The reason for this is the dissipation; the situation is similar to the fact that a viscous extension of the Burgers equation yields stability of shocks only with $u_- > u_+$.

For $u_- < u_+$ a rarefaction wave occurs in the solution of the Burgers equation and again the solution of the system (17) follows the rarefaction wave, but is does have a diffusive profile. We will not go into the details of that case.

The denominator in (27) has the form of the characteristic polynomial (18) of the system. Whenever a characteristic velocity inside the shock reaches the shock velocity, the gradient of $\widehat{u}$ becomes infinite. The function $\xi\left(\widehat{u}\right)$ has a extreme point and $\widehat{u}\,(\xi)$ becomes non-unique. In the solution for the travelling wave a sub-shock occurs. This behavior is typical for dissipative hyperbolic systems and we will come back to it in Sect. 4.3.

4.2 Relaxational solution

For very small times the productions in (17) have no influence and the solution of the Riemann problem (20) consists of the two characteristic waves corresponding to the two velocities (19). Afterwards these waves are damped at a rate that depends on the value of the parameter B. Thus these waves are best observed by looking at the solution for a fixed time and varying the parameter B.

In Fig.2 we see the solution of (17) for the fixed time $t = 0.4$ and different values of B, viz.

$$B = 0, 1, 2, 5, 10, 20, 50, 100, 500.$$

All of these solutions start for small times with the two characteristic waves and (except for $B = 0$) converge to a travelling wave for large times. For some large values of B the steady profile is already established at the time shown.

In the case $B = 0$ the non-dissipative homogeneous system (17) is solved. In the solution two discontinuities or shocks[1] arise, which travel to the right and to the left with a constant state in between. This solution

[1] One has to be careful with the label 'shock' since the travelling wave also represents a shock, but with a diffusive shock structure. Here the term shock is used only, if discontinuities occur.

does not change shape. It only moves according to the typical x/t-dependence. For $B \neq 0$, however, the discontinuities loose strength, they are damped by the dissipation. The curve becomes smooth and forms the shock structure. In the limit of large B the profile becomes steeper and steeper indicating that the Burger equation with its shock solution is recovered in the system (17). This is a scaling effect: For a given B the eventual steady profile remains steady with time, but the length scale is influenced by the parameter B, so the profile *appears* to be very steep. This effect of B becomes more clear in the results of the 13-field-case in Sect.5.

The two shocks of the starting solution may be calculated from the Rankine-Hugoniot-relations for the system (17). These read

$$\frac{1}{2}u_+^2 + 2\sigma_+ - \frac{1}{2}u_-^2 - 2\sigma_- = s\left(u_+ - u_-\right) , \tag{29}$$

$$u_+ - u_- = s\left(\sigma_+ - \sigma_-\right) . \tag{30}$$

The shock speed is denoted by s, and $\left(u_-, \sigma_-\right)$ and (u_+, σ_+) are the left- and right-hand states of the discontinuity. From (29) and (30) the shock speeds are given by

$$s_{1,2} = \frac{u_+ + u_-}{4} \pm \sqrt{\frac{\left(u_+ + u_-\right)^2}{16} + 2} . \tag{31}$$

We introduce the shock strength α by

$$u_+ = (1+\alpha)\, u_- , \tag{32}$$

$$\sigma_+ = (1+\alpha)\, \sigma_- , \tag{33}$$

so the speeds $s\left(\alpha; u_-, \sigma_-\right)$ are functions only of one state and the shock strength. The Hugoniot loci $H_{1,2}$ of admissible 1- and 2-shocks in the phase plane (u, σ) are obtained from (29)/(30) with (31)

$$H_{1,2}\left(\alpha; u_-, \sigma_-\right) = \begin{pmatrix} u_+ \\ \sigma_+ \end{pmatrix} = \begin{pmatrix} 2s_{1,2}(\alpha) - \dfrac{4}{s_{1,2}(\alpha)} - u_- \\ \sigma_- + 2 - \dfrac{4}{s_{1,2}(\alpha)^2} - \dfrac{2u_-}{s_{1,2}(\alpha)} \end{pmatrix} . \tag{34}$$

In Fig. 3 these curves are depicted in the (u, σ)-plane for the Riemann problem given by (20). In $(1, 0)$ an 1-shock starts and in $(2.5, 0)$ a 2-shock. It is easily verified that for both shocks the Lax condition

$$\lambda_{1,2}^- > s_{1,2} > \lambda_{1,2}^+ \tag{35}$$

holds. The dashed lines in Fig. 3 correspond to the solutions shown in Fig. 2. The damped discontinuities follow their Hugoniot locus down to zero strength. Thus not only the strength but also the speed of the shocks is affected by the damping, a fact that may be read off Fig. 2. For large B the solution converges to the limiting cyclus of the travelling wave given by (25). It is remarkable that the non-equilibrium variable σ does not tend to zero for large B. Again the scaling effect takes over so that σ vanishes almost everywhere.

The structure of the production in (17) shows that the shocks are damped exponentially. They will not disappear in finite times. Nevertheless the solution of the travelling wave in (28) is smooth, since the ansatz (21)/(22) assumes an infinite far away start-up phase.

4.3 Subshock solution

A subshock arises in the travelling wave solution, if the discontinuity from the start-up phase is not fast enough to run away from the emergent profile of the travelling wave.

The initial conditions

$$u(x, t=0) = \begin{cases} 3.5 & x \leq 0 , \\ 1 & x > 0 , \end{cases} \qquad \sigma(x, t=0) = 0 \tag{36}$$

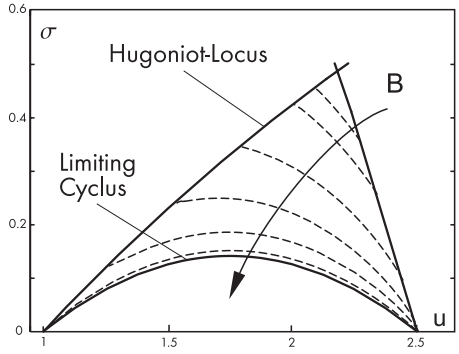

Fig. 3. Solution of (17) in the phase plane

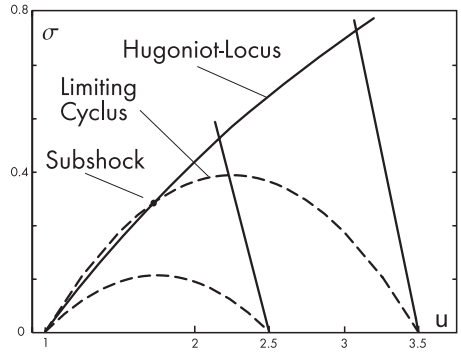

Fig. 4. Subshock solution in the phase plane

produce a shock structure that moves with the velocity

$$v = \frac{u_+ + u_-}{2} > \lambda_1 (u = 1) \ , \tag{37}$$

which is greater than the characteristic velocity at $u = 1$. In Fig. 4 we see the Hugoniot locus as well as the limiting cyclus for the Riemann problem given by (36) together with the earlier one (20). The limiting cyclus for (36) now intersects with the Hugoniot locus of the 1-shock. The intersection point may be calculated by (34) and (25) and is given by

$$(u_s, \sigma_s) = (1.72, 0.32) \ . \tag{38}$$

The solution has a subshock from $(1, 0)$ to (u_s, σ_s) and then follows the smooth limiting cyclus. With this background the subshock may be viewed as a discontinuity from the start-up phase that cannot be damped below a certain strength.

In Fig. 5 the analytical and numerical solution of (36) are shown.

The numerical solution has significant problems to resolve the subshock. In particular, if one compares this result with the resolution of the discontinuities in the case of $B = 0$. The solution in Fig. 5 has been made with a grid width $\Delta x = 1/350$ on the interval $[-0.6, 1.4]$.

5 Results of the 13-field-case

We consider the Riemann problem for the 13-field-case with the initial conditions

$$\begin{aligned} \rho(x, t = 0) &= \begin{cases} \rho_1 \ , & x \leq 0 \ , \\ \rho_0 \ , & x > 0 \ , \end{cases} \\ p(x, t = 0) &= \begin{cases} p_1 \ , & x \leq 0 \ , \\ p_0 \ , & x > 0 \ , \end{cases} \end{aligned} \qquad \begin{aligned} v(x, t = 0) &= 0 \ , \\ \sigma(x, t = 0) &= 0 \ , \\ q(x, t = 0) &= 0 \end{aligned} \tag{39}$$

and solve the equations of the 13-field-case as well as the Euler case. This problem is known as Sod's problem [16] in the numerical literature. It describes a simple shock-tube-experiment with a gas initially at rest and in

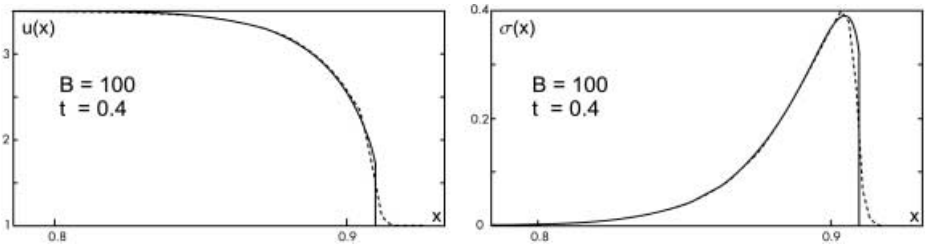

Fig. 5. Analytical (solid) and numerical (dashed) solutions of (36)

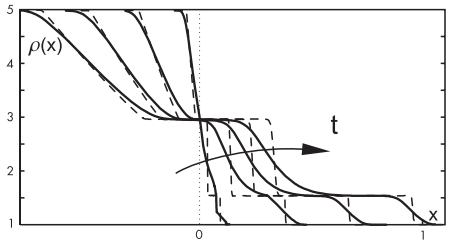

Fig. 6. Density of the 13-field-case (solid) and the Euler case (dashed) for different times

equilibrium, but separated into a high pressure and a low pressure region. As reference state the low pressure state ρ_0, p_0 is chosen. The pressure and density ratios are

$$\frac{\rho_1}{\rho_0} = 5\,, \qquad \frac{p_1}{p_0} = 5\,. \tag{40}$$

It follows with the ideal gas law $p \sim \rho T$ that the temperature is initially constant $T_1 = T_0$.

For the Euler case there exists an analytical solution (see [5], [6]) for (39). With the ratios (40) it consists of two discontinuities travelling to the right and a rarefaction wave, which fans out to the left. From (40) we may conclude that the fast shock has the velocity

$$s = 1.369\sqrt{\frac{5}{3}\frac{p_0}{\rho_0}}\,,$$

that is a Mach number $M = 1.369$. The second discontinuity is the contact discontinuity, which moves with the gas velocity v. All three waves can be observed in the experiments.

In Fig. 6 the solution of the density field of the 13-field-case is shown for different times and a fixed parameter $B = 125$. Also the solution of the Euler case is shown. The 13-field-case exhibits the same behavior as the model system in Fig. 1: After a start-up phase the solution follows the Euler solution with diffusive profiles. These diffusive profiles have a higher physical significance than the discontinuities in the Euler case for the following reason: From the definition of B in (6) we see that by choosing its value we choose a time as well as a length scale. Thus $x = 1$ in Fig. 6 correspond to about 100 mean free paths. At that scale we resolve the diffusive structure of the shock which is spread over several mean free pathes. The Euler equations are only valid for $B \to \infty$ or $Kn \to 0$; in that case the shock structure *appears* as discontinuity. This corresponds to the scaling effect which seems to steepen the profile in Fig. 2.

The shock structure form a travelling wave which may be calculated separately [17]. The profile of the contact discontinuity is not steady, it is smeared out very slowly with time due to heat conduction.

In Fig. 7 we see the fields of density ρ, pressure p and velocity v for the 13-field-case and the Euler case for a fixed time but different values of B. Varying the parameter B now means looking at the solution at different physical time and length scales. In the figure space is measured in mean free paths of the reference state λ. The solution of the Euler equations shows the same shape at any scale due to its self similarity. For $B = 0$ the scale is infinitesimally small and we solve the Riemann problem of the homogeneous system (5). The solution shows five characteristic waves according to the five characteristic velocities (10). There are two rarefaction waves and three discontinuities. The solution has almost nothing in common with the solution of the Euler equations. Due to the dissipation in the system (5) the discontinuities loose strength and the rarefaction waves are smoothed out. Again it may be observed that the discontinuities become slower while

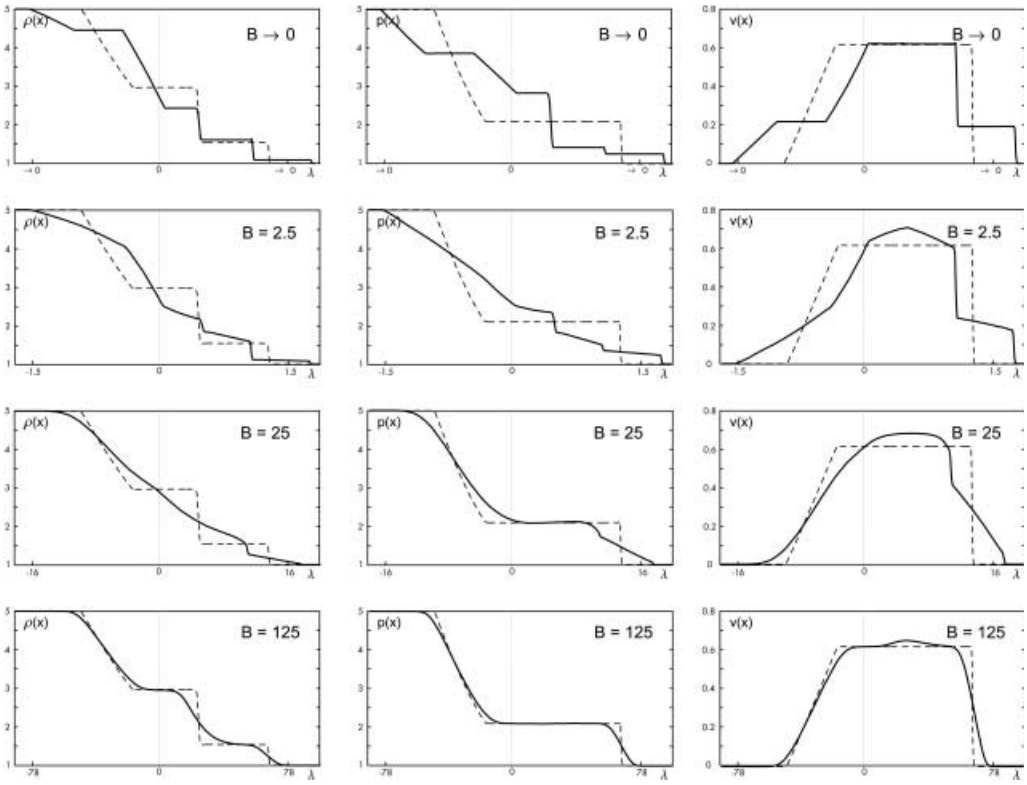

Fig. 7. Fields of density, pressure and velocity in the 13-field-case (solid) and the Euler case (dashed)

being damped. After a certain time the curves follow the solutions of the Euler equations. It seems remarkable that this happens. In Sect.4.1 we saw that the shock structure travels with the shock speed of the underlying Burgers equation even for finite B. In Fig. 7 we see that the 13-field-case recognizes the propagation of the contact discontinuity as well as of the rarefaction wave, which move according to the characteristics of the Euler system, although these characteristics are absent in the 13-field-case.

In Fig. 8 the corresponding fields of stress σ and heat flux q are shown together with the density field. In these fields too the five characteristic waves are present in the beginning. Remarkable is the non-monotone shape of the slow rarefaction wave in the stress. Once again the waves are damped and the result is a soliton-like solution, indicating the non-equilibrium across the structures of the shock, the contact discontinuity and - much less - across the rarefaction wave.

The waves of the 13-field-case for small B have no physical significance. In particular the disturbance that propagates at $1.65\sqrt{p/\rho}$ has never been observed. For a physical description of the start-up phase one will need many more variables than 13, because of the strong non equilibrium. This will be shown in a future paper [18].

If the Mach number of the shock structure exceeds 1.65, - which is the highest characteristic velocity - it appears a subshock within the structure. Unfortuntely it is not possible to calculate such a structure by solving a Riemann problem of the type (39)/(40): For a slightly higher initial pressure ratio the solution leaves the region of hyperbolicity.

5.1 Region of hyperbolicity

The 13-field-case is not globally hyperbolic, due to linearisation during the derivation of the system. For a given equilibrium state ρ, p only a certain range of values of stress σ and heatflux q close to equilibrium are allowed. Outside of this range the characteristic polynomial (9) has imaginary roots. If the stress and the heat flux are made dimensionless with the given equilibrium state

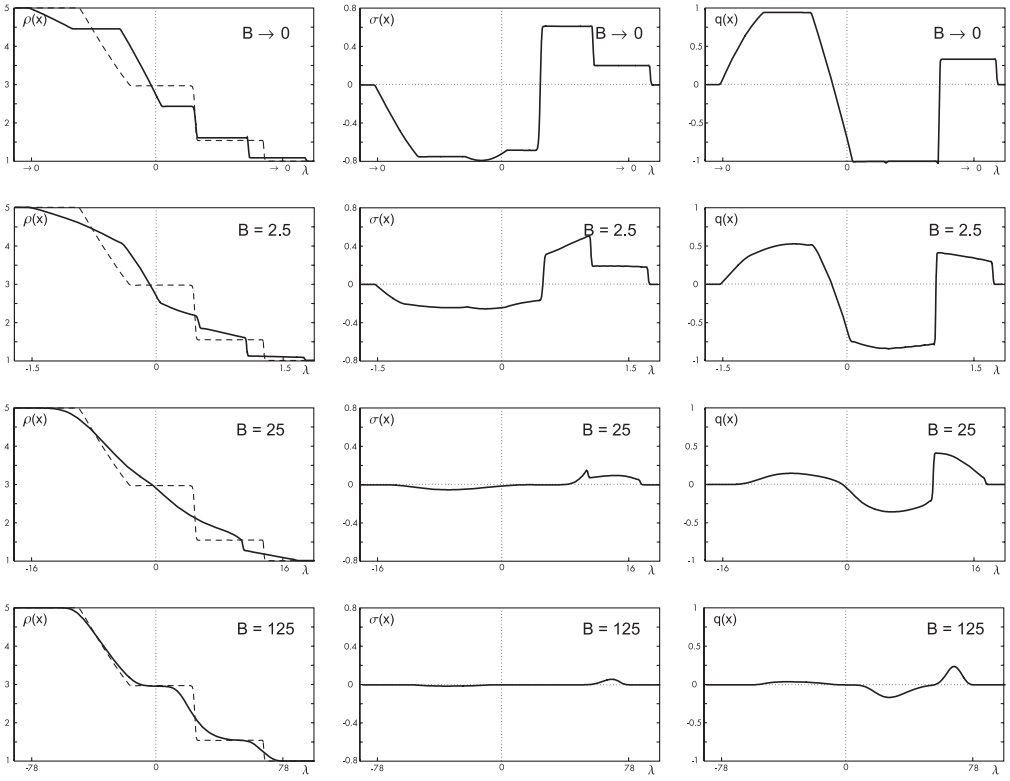

Fig. 8. Fields of density, stress and heat flux in the 13-field-case

$$\widetilde{\sigma} = \frac{\sigma}{p}, \tag{41}$$

$$\widetilde{q} = \frac{q}{p\sqrt{\frac{p}{\rho}}} \tag{42}$$

we may draw a region of hyperbolicity in the $(\widetilde{q}, \widetilde{\sigma})$-plane. The borderline of the region of hyperbolicity is given by the functions (see [1])

$$\widetilde{q}\,(\widetilde{\sigma}) = \pm\frac{1}{972}\sqrt{\frac{5}{3}}\,(117 + 93\,\widetilde{\sigma} - D\,(\widetilde{\sigma}))\,\sqrt{117 + 93\,\widetilde{\sigma} + 2\,D\,(\widetilde{\sigma})} \tag{43}$$

with

$$D\,(\widetilde{\sigma}) := \sqrt{8541\,\widetilde{\sigma}^2 + 14553\,\widetilde{\sigma} + \frac{15957}{2}}\,. \tag{44}$$

Both curves are shown in Fig. 9 as dashed lines.

Additionally we see the results of the 13-field-case for the Riemann problem (39) with (40) and different values of B in the first row of Fig. 9. The curves are parametrized by the space variable x and read

$$s\,(x) = \begin{pmatrix} \dfrac{\sigma\,(x)}{p\,(x)} \\ \dfrac{q\,(x)}{p\,(x)\sqrt{\frac{p(x)}{\rho(x)}}} \end{pmatrix}. \tag{45}$$

They are closed and begin and end in an equilibrium state, which occurs in the origin of the $(\widetilde{q}, \widetilde{\sigma})$-plane. In the case of $B = 0$ we see a polygon, whose five legs represent the five characteristic waves. Due to the damping the polygon collapses as B grows and forms a small steady loop which indicates mainly the dissipation in the shock structure. In the second row of Fig. 9 the polygon in the case of $B = 0$ for different initial pressure

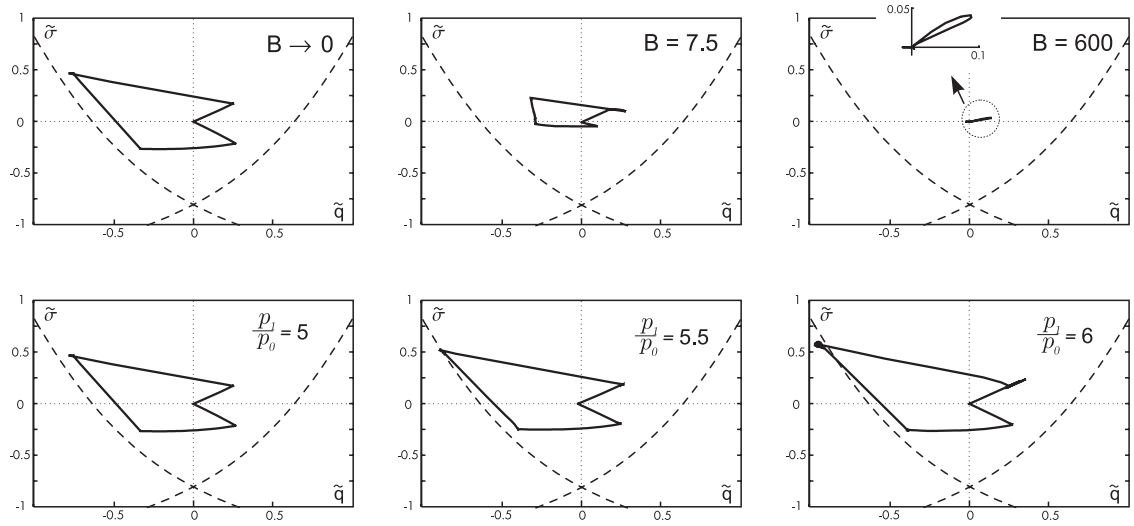

Fig. 9. Several solutions of the 13-field-case in the hyperbolicity region

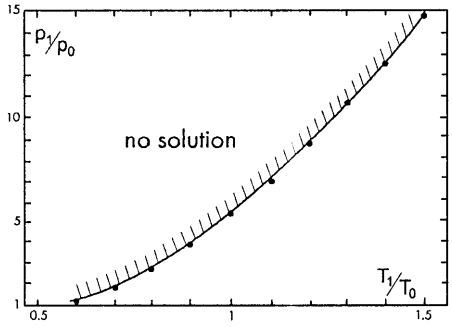

Fig. 10. Boundary of existing solutions for the Riemann problem (39)

ratios is shown. The density ratio is assumed to be equal to the pressure ratio, which implies constant initial temperature. For a pressure ratio of 6 the curve $s(x)$ leaves the region of hyperbolicity. Of course damping would reestablish hyperbolicity after a short time, but immediately after the loss of hyberbolicity the upwind method breaks down. The solution in Fig. 9 has been calculated by a central method [19] that does not rely on the eigenstructure of the equations.

For a given temperature ratio, one can numerically check different pressure ratios and find out when the first imaginary roots appear. The result is shown in Fig. 10. The dots mark the verified marginal pressure ratios within ± 0.05 and the curve is a arbitrary fit. Above that curve no solution of the homogenous 13-field-case for the Riemann problem (39) is possible due to the loss of hyperbolicity.

The results in Fig. 10 were observed to change slightly, if the grid is refined. I used a grid width of $\Delta x = 1/200$ on an interval $[-1.5, 1.5]$ which gave relieable results.

References

1. Müller I, Ruggeri T (1998) Rational Extended Thermodynamics (2nd edn), Springer Tracts in Natural Philosophy (vol.37), Springer, New York
2. Weiss W (1990) Zur Hierarchie der Erweiterten Thermodynamik, dissertation, TU Berlin
3. Liu TP (1987) Hyperbolic Conservation Laws with Relaxation, Comm. Math. Phys. **108**, p.153
4. Courant R, Friedrichs KO (1976) Supersonic Flow and Shock Waves, Applied Mathematical Science (vol. 21), Springer, New York
5. Shapiro AH (1954) Compressible Fluid Flow (vol II), Ronald Press Company, New York
6. Toro EF (1999) Riemann Solvers and Numerical Methods for Fluid Dynamics (2nd edn), Springer, Berlin
7. Russo G (2000) Central Schemes for Balance Laws, Proc. 8th Int. Conf. Hyp. Probl., Magdeburg, in press
8. Groth CPT, Roe PL, Gombosi TI, Brown SL (1995) On the Nonstationary Wave Structure of a 35-Moment Closure for Rarefied Gas Dynamics, AIAA Paper 95–2312

9. LeVeque RJ: CLAWPACK – A Package for Solving Conservation Laws, source available in www.amath.washington.edu/˜rjl/clawpack.html
10. LeVeque RJ (1992) Numerical Methods for Conservation Laws (2nd edn), Lectures in Mathematics, ETH Zürich, Birkhäuser Verlag, Basel
11. Strang G (1968) On the Construction and Comparison of Difference Schemes, SIAM J. Num. Anal. **5**, p. 506
12. Hairer E, Wanner G: Numerical Solver for Differential Equations, source available in www.unige.ch/math/folks/hairer/software.html
13. Roe PL (1981) Approximate Riemann Solvers, Parameter Vectors and Difference Schemes, J. Comp. Phys. **43**, p. 357
14. Numerical Algorithm Group Ltd (1995) Fortran 77 Libraries, Mark 18, Oxford
15. Harten A, Hyman JM (1983) Self Adjusting Grid Methods for One-Dimensional Hyperbolic Conservation Laws, J. Comp. Phys. **50**, p. 235
16. Sod GA (1978) A Survey of Several Finite Difference Methods for Systems of Nonlinear Hyperbolic Conservation Laws, J. Comp. Phys. **27**, p. 1
17. Weiss W (1995) Continuous Shock Structure in Extended Thermodynamics, Phys. Rev. E 52, p. 5760
18. Torrilhon M, Au JD , Weiss W: The Shock-Tube-Study in Extended Thermodynamics, in preparation
19. Nessyahu H, Tadmor E (1990) Non-oscillatory Central Differencing for Hyperbolic Conservation Laws, J. Comp. Phys. **87**, p. 408